ISSUES IN THE MECHANICAL ENGINEERING DESIGN OF HIGH-PRECISION KINEMATIC COUPLINGS

Saša Zelenika[1, 2*] – Kristina Marković[1, 2] – Josipa Rubeša[3]

[1]Department of Mechanical Engineering Design, Faculty of Engineering, University of Rijeka, Vukovarska 58, 51000 Rijeka, Croatia
[2]Center for Micro- and Nanosciences and Technologies, University of Rijeka, Radmila Matejčić 2, 51000 Rijeka, Croatia
[3]Almes, Pomerio 9, 51000 Rijeka, Croatia

ARTICLE INFO

***Article history*:**
Received: 26.4.2016.
Received in revised form: 20.5.2016.
Accepted: 23.5.2016.

Keywords:
Hertzian contacts
High-precision
Kinematic mounts
Stability
Modelling

Abstract:

A three V-groove (Maxwell-type) kinematic mount design configuration constrains all degrees of freedom of the apparatus mounted onto it, thus allowing its high-precision positioning and re-positioning. The analysis of this mechanical assembly comprises force and moment balances, as well as expressions for stress-strain and error motion calculations. For determined loading conditions and the geometry of the mount, the resulting loads across each groove-ball interface imply, however, the necessity to consider the complex nonlinear Hertz theory of point contacts between elastically deforming solids. The available analytical approaches to the calculation of the conditions at the ball-V groove contacts are hence recalled in this work with the aim of establishing the respective limits of applicability. The obtained results are validated experimentally. A structured calculation procedure is then used to assess the stability of a kinematic mount employed to support a large mechanical component at a particle accelerator facility, depending on the value and orientation of the external loads acting on the studied assembly. Stability conditions for different design configurations are consecutively established.

1 Introduction

In the design of machine elements (e.g. gear teeth contacts, ball bearings' contacts, ball screws, … – cf. e.g. [1-2]), the designers are often confronted with the need to consider point contacts, which, if calculated strictly canonically, are difficult to compute since the calculation implies the necessity to consider the nonlinear Hertz theory of point contacts between elastically deforming solids [3]. In precision engineering, this problem is especially evident in the case of the so-called kinematic mounts that are used in high-precision applications since they are self-locating and free from backlash,

* Corresponding author. Tel.: + 385 – (0)51 – 651538; fax: + 385 – (0)51 – 651416
E-mail address: sasa.zelenika@riteh.hr.

allowing thus the sub-micrometric positioning and re-positioning of the coupled mechanical elements in both static and dynamic applications. What is more, kinematic mounts allow for accommodating differential thermal expansions, whereas their behaviour in terms of the force and moment equilibria, thus comprising the calculation of the stress-strain conditions at the contact points, can be represented in a closed form solution [4].

The most common kinematic mount design configuration is the Maxwell-type mount constituted by three V-grooves on the support and three balls on the supported piece, so as to achieve an exact constraint of all six spatial degrees of freedom (DOFs – Fig. 1).

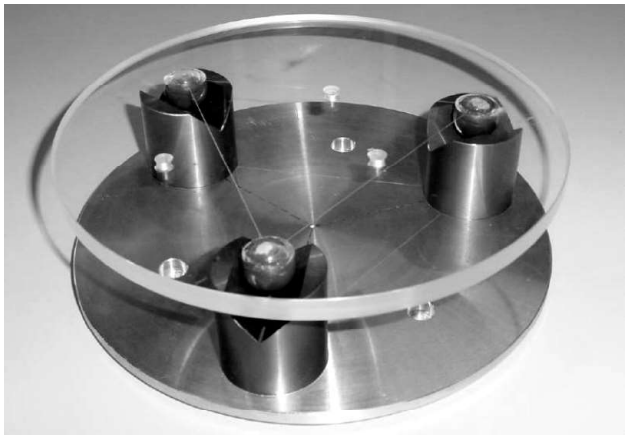

Figure 1. Maxwell kinematic mount.

The aim of this work is to analyse the influence of the mechanical design parameters on the stress-strain behaviour (related to the resulting positioning precision) and the stability of the considered class of kinematic mounts. A factual example of a mount used to support a large structure at a particle accelerator facility is then considered. Stability conditions for different design configurations are established.

2 Analytical model of the contacts in the Maxwell-type kinematic couplings

Based on the pioneering work of James Clerk Maxwell in 1876, the analysis of a Maxwell-type kinematic mount comprises force and moment balance equations, expressions for the calculation of stresses and deflections at the contact points and error motion calculation. Knowing the external loads (including the preload) and the geometry of the coupling, the reactions at each groove-ball interface can be computed from the overall force and moment balances [4]. Obviously, across each interface between the ball and V-groove, there are two contact points (Fig. 2) so that the whole mount results in six contact points, thus constraining all the DOFs of the elements joined by the coupling.

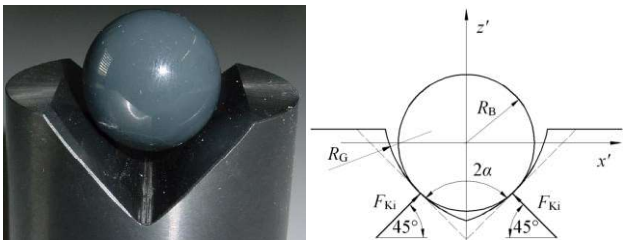

Figure 2. Ball – V-groove interface.

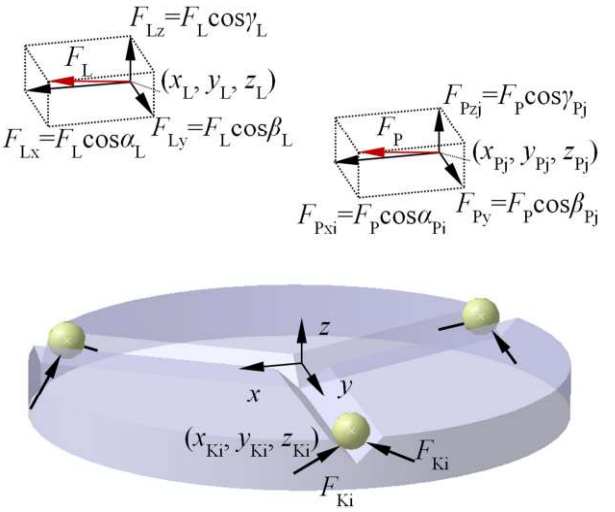

Figure 3. Information required to define a three V-groove kinematic coupling.

The input to the calculation is hence [4] (cf. Figs. 3 and 4):

- the balls' and grooves' radii R_B and R_G,
- the coordinates x_{Ki}, y_{Ki} and z_{Ki} of the contact points of the balls in the grooves with the respective direction cosines α_{Ki}, β_{Ki} and γ_{Ki} of the contact forces,
- the preload force F_{Pj} (the weight resting on the support) with the respective coordinates x_{Pj}, y_{Pj} and z_{Pj} and direction cosines α_{Pj}, β_{Pj} and γ_{Pj},
- the externally applied load F_L with the respective coordinates x_L, y_L and z_L and direction cosines α_L, β_L and γ_L (the effect of more loads can be evaluated using superposition),

- the modules of elasticity and Poisson ratios of the ball and groove materials.

On the other hand, the output from the analysis is obtained in terms of [4]:

- the contact forces F_{Ki} and contact stresses q_i at each of the six contact points,
- the deflections δ_i at each of the contact points,
- the translational errors δ_X, δ_Y and δ_Z of any point G (x, y, z) in space around the coupling.

Hertz theory describes the nonlinear behaviour of point contacts between elastic isotropic solids loaded perpendicular to the surface where the contact area is small compared to the radii of curvature and the dimensions of the involved bodies. The respective analytical model entails a lengthy iterative evaluation of transcendental equations involving elliptic integrals [5]. In fact, by indicating the Young's moduli and the Poisson's ratios of the bodies in contact with E_1, ν_1, E_2, and ν_2, the ball radius with R_B, and the groove radii (Fig. 4), with R_{G1} ($R_{G1} = -R_B\,(1+\gamma)$) and R_{G2} ($R_{G2} = \infty$) the following notation can be introduced [5]:

- equivalent Young's modulus of the system:

$$E_{ekv} = \frac{1}{\frac{1-\nu_1^2}{E_1} + \frac{1-\nu_2^2}{E_2}} \tag{1}$$

- equivalent radius of curvature:

$$R_{ekv} = \frac{R_B(1+\gamma)}{1+2\gamma} \tag{2}$$

γ is here the ball-groove radius ratio which affects the contact stresses and the resulting deflections. To avoid problems with contamination of the contact zone, γ should be as large as possible. On the other hand, to minimize the effect of contact stresses and deflections, it should be as small as possible. A practical optimal value suggested in literature is hence $\gamma = 0{,}2$ [4].

In the general case, the geometry of the contact has an elliptic shape (Fig. 5) with a ratio of the respective major and minor semi-axes lengths:

$$k = \frac{c}{d} \geq 1 \tag{3}$$

whereas the values of the semi-axes lengths, the resulting interpenetration distance δ of the bodies in contact (i.e. the deflection of the contact points) and the maximum contact stress q_{max} can be defined as:

$$c = \alpha \sqrt[3]{\frac{3F_{Ki}R_{ekv}}{2E_{ekv}}} \tag{4}$$

$$d = \beta \sqrt[3]{\frac{3F_{Ki}R_{ekv}}{2E_{ekv}}} \tag{5}$$

$$\delta = \lambda \sqrt[3]{\frac{2F_{Ki}^2}{3R_{ekv}E_{ekv}^2}} \tag{6}$$

$$q_{max} = \frac{3F_{Ki}}{2\pi cd} \tag{7}$$

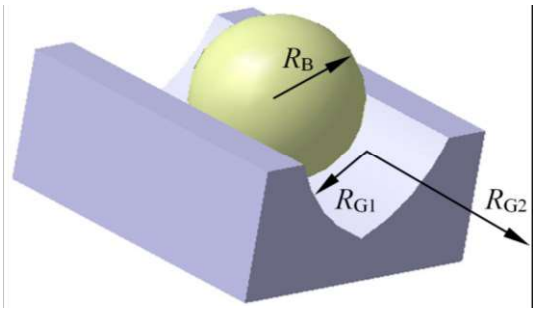

Figure 4. Contact interface geometry.

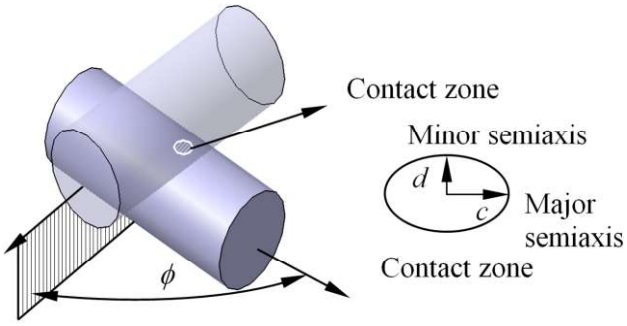

Figure 5. Contact zone.

In exact expressions for calculating these values, i.e., the ones of the characteristic parameters α, β and λ, there is the evidenced problem of the need to resort to a cumbersome and computationally intensive repetitive calculation of the values of the complete elliptic integrals of the first and second kind [6-7]. . The relations for the calculation of the geometry, the deflections and the stresses in the contact region, obtained by employing the approximated methods suggested in literature, in

which the need to calculate the elliptic integrals is obviated by introducing polynomial [4], tabular [8-9] or graphical [10-11] representations of the characteristic parameters are, in turn, summarized in Table 1. Here a represents the radius of the equivalent circular contact area (obtained by reduction of the exact elliptic area), $\cos\theta$ is dependent on the radii of curvature and ϕ – the angle between the planes of principal curvature (Fig. 5), while other parameters are analogous to those given above.

Table 1. Approximated analytical methods

	pol. approx. [4]	interp. [8]	interp. [9]	diagrams [11]	diagrams [10]	gap-bending [4]
R_{ekv}	$R_B\frac{1+\gamma}{1+2\gamma}$	$2R_B\frac{1+\gamma}{1+2\gamma}$	$1,5R_B\frac{1+\gamma}{1+2\gamma}$	$R_B\frac{1+\gamma}{1+2\gamma}$	$4R_B\frac{1+\gamma}{1+2\gamma}$	$R_B\frac{1+\gamma}{1+2\gamma}$
$\cos\theta$	$\frac{R_{ekv}}{\lvert R_G\rvert}$	$\frac{R_{ekv}}{2\lvert R_G\rvert}$	$\frac{R_{ekv}}{1,5\lvert R_G\rvert}$	$\frac{R_{ekv}}{\lvert R_G\rvert}$	$\frac{R_{ekv}}{4\lvert R_G\rvert}$	/
c	$\alpha\sqrt[3]{\frac{3F_{Ki}R_{ekv}}{2E_{ekv}}}$	$\alpha\sqrt[3]{\frac{3F_{Ki}R_{ekv}}{4E_{ekv}}}$	$\alpha\sqrt[3]{\frac{3F_{Ki}R_{ekv}}{E_{ekv}}}$	$\alpha\sqrt[3]{\frac{3F_{Ki}R_{ekv}}{E_{ekv}}}$	$\alpha\sqrt[3]{\frac{3F_{Ki}R_{ekv}}{8E_{ekv}}}$	$a=\sqrt[3]{\frac{3F_{Ki}R_{ekv}}{2E_{ekv}}}$
d	$\beta\sqrt[3]{\frac{3F_{Ki}R_{ekv}}{2E_{ekv}}}$	$\beta\sqrt[3]{\frac{3F_{Ki}R_{ekv}}{4E_{ekv}}}$	$\beta\sqrt[3]{\frac{3F_{Ki}R_{ekv}}{E_{ekv}}}$	$\beta\sqrt[3]{\frac{3F_{Ki}R_{ekv}}{E_{ekv}}}$	$\beta\sqrt[3]{\frac{3F_{Ki}R_{ekv}}{8E_{ekv}}}$	$a=\sqrt[3]{\frac{3F_{Ki}R_{ekv}}{2E_{ekv}}}$
δ	$\lambda\sqrt[3]{\frac{2F_{Ki}^2}{3R_{ekv}E_{ekv}^2}}$	/	$\lambda\sqrt[3]{\frac{2F_{Ki}^2}{R_{ekv}E_{ekv}^2}}$	$\lambda\sqrt[3]{\frac{2F_{Ki}^2}{R_{ekv}E_{ekv}^2}}$	$\lambda\sqrt[3]{\frac{2F_{Ki}^2}{64R_{ekv}E_{ekv}^2}}$	$\frac{1}{2}\sqrt[3]{\frac{9F_{Ki}^2}{4R_{ekv}E_{ekv}^2}}$
q_{max}	$\frac{3F_{Ki}}{2\pi cd}$	$\frac{3F_{Ki}}{2\pi cd}$	$\frac{3F_{Ki}}{2\pi cd}$	$\gamma\sqrt[3]{\frac{F_{Ki}E_{ekv}^2}{R_{ekv}^2}}$	$\frac{3F_{Ki}}{2\pi cd}$	$\frac{aE_{ekv}}{\pi R_{ekv}}$

The results of the calculation of the behaviour in the contact region obtained for the considered ball-V groove case by using the approximated analytical methods of Table 1 are hence compared in Fig. 6. For clarity reasons, the results are given as differences of each of the considered method with respect to the exact solution. It can thus be observed that, with exception of the gap-bending hypothesis [4], which introduces considerable errors, the errors introduced by the approximated methods based on polynomial, tabular and graphical representations are always smaller than ± 2% (or even, for the methods given in [8-9], smaller than ± 0,2% – Fig. 6). Given the small entity of the stresses and strains involved in most high-precision applications, these errors can hence be considered negligible in all but those cases where true nanometric accuracies are sought. Only in the case when the mentioned characteristic parameters approach their limit values (respectively 0 and ∞), which physically corresponds to the curvature of the groove approaching that of the ball, become the errors involved in the approximated methods appreciable. In this case, however, Hertz theory itself starts to break down [6].

To validate these results, an experimental set-up was built (Fig. 7). Stainless steel and ceramic (tungsten carbide (WC) and silicon nitride (Si_3N_4)) polished balls and gothic-arch grooves are hence employed. It is thus proven that in the whole elastic deformations range, the correspondence of the theoretical values of the interpenetration distances δ with the experimental ones is within the intervals of uncertainty of the latter, regardless of the used materials and lubrication conditions. Moreover, the precision of the Maxwell-type kinematic mounts is shown to be comparable to the surface finish of the coupling interface (100 nm range), i.e., it is in the nanometric domain – Fig. 8 [6].

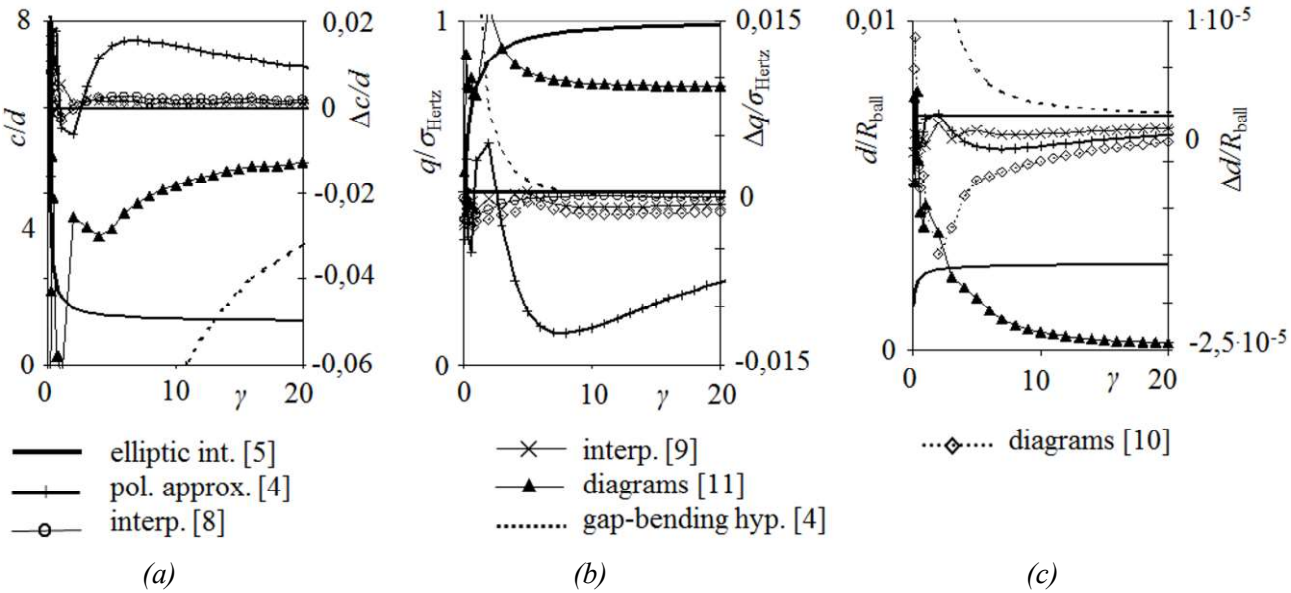

(a) *(b)* *(c)*

Figure 6. Ratio of the semi-axes lengths of the elliptical contact area (a), normalized contact stresses (b) and normalized interpenetration distances (c) versus the ratio of the radii of curvature γ.

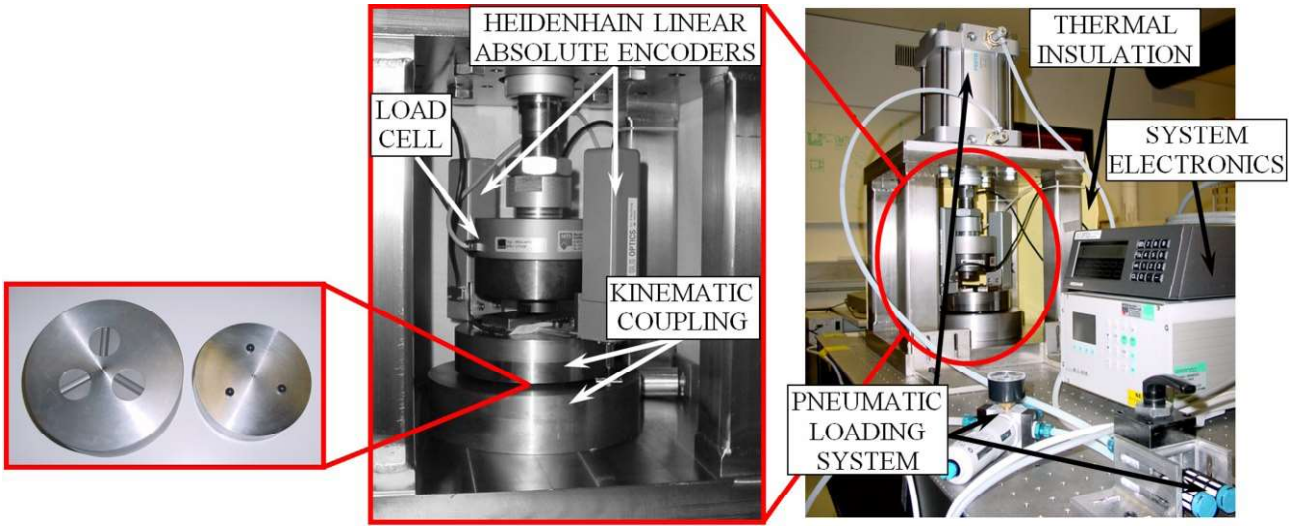

Figure 7. Experimental set up.

In the calculations used in the following treatise, the behaviour of the considered kinematic coupling design configurations will therefore be performed based on the polynomial approximation method suggested in [4] where the characteristic parameters for the evaluation of the contact region are defined as:

$$\alpha = 0,99672 + 1,2786\cos\theta - \\ -607201\cos^2\theta + 27,379\cos^3\theta - \\ -41,827\cos^4\theta + 23,472\cos^5\theta \quad (8)$$

$$\beta = 1 - 0,68865\cos\theta + \\ +0,58909\cos^2\theta - 1,3277\cos^3\theta + \\ +1,7706\cos^4\theta - 0,99887\cos^5\theta \quad (9)$$

$$\lambda = 0,75018 - 0,04213\cos\theta + \\ +0,29526\cos^2\theta - 1,7567\cos^3\theta + \\ +2,6781\cos^4\theta - 1,5533\cos^5\theta \quad (10)$$

One of the most relevant boundary conditions in the resulting calculations is certainly that of the maximal allowable stresses. In fact, to prevent

surface damage, the contact pressure induced by the maximal calculated contact forces must be lower than the allowable Hertzian contact stress. Depending on the material used for the production of the balls and the V-grooves, the contact stress for metal and ceramic elements of the coupling can be calculated as [4]:

$$\sigma_{\text{Hmax METAL}} = \frac{3\sigma_{\text{ALLOWABLE TENSILE STRESS}}}{2}$$
$$\sigma_{\text{Hmax CERAMIC}} = \frac{2\sigma_{\text{ALLOWABLE FLEXUAL STRESS}}}{1-2\nu} \quad (11)$$

In this work, an additional safety margin of 30% with respect to the thus calculated Hertzian contact stress is assumed.

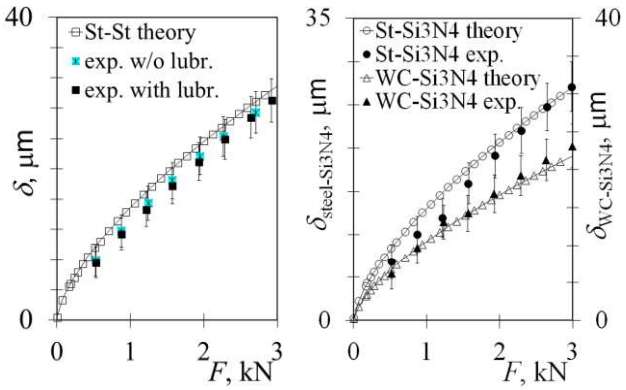

Figure 8. Theoretical and experimental values of interpenetration distances δ.

3 Analysis of the stability of the Maxwell-type kinematic mounts

Considering in the next step the equilibrium of the overall Maxwell-type kinematic mount, the products of the absolute deflection of the balls with the direction cosines of the contact forces are used to calculate the components of ball deflections. It is here implicitly assumed that, due to a finite coefficient of friction at the contact interface, there is no relative motion between the ball and the groove. Moreover, it is also assumed that the change of the distance between the balls induced by their deflections is much smaller than the deflection at the contact points. The displacement of the coupling triangle's centroid (Fig. 9) is hence assumed to be equal to the weighted average of the deflections of the balls [4].

Therefore, the errors induced by the rotation of the whole coupling, assuming that they are small, can be assembled in a homogenous transformation matrix. The resulting translational errors of any point in space around the coupling can finally be determined [4].

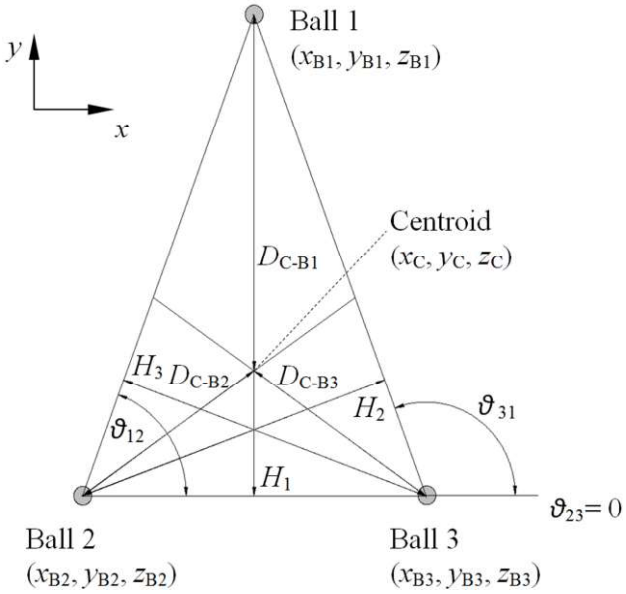

Figure 9. Top view of the geometry of the mount.

In the case of symmetric design configurations of the Maxwell-type kinematic mount where its contacts, i.e., the vertices of the coupling triangle, are so positioned as to create an equilateral triangle, and consequently a good stability of the coupling will be guaranteed, as shown in Fig. 10, when the normals to the planes containing the contact force vector pairs bisect the angles between the balls. Also, for balanced stiffness in all directions, the contact force vectors should intersect the plane of coupling action at an angle of 45° (cf. Fig. 2 right) [4].

When the apparatus supported by the coupling is subject to the action of an external load (possibly of varying directions), the stability of the coupling must, in turn, be checked by controlling if all the values of the contact forces are positive, i.e. that there is no tendency of lifting the supported structure from the coupling. In this case, a general requirement of trying to balance the stiffness in all directions is set, while maintaining the stresses in the allowable region. These requirements may imply the need to modify the aspect ratio of the coupling triangle. Two cases are generally

considered in this instance:

- the case when the normals to the planes containing the contact force vectors always point towards the coupling centroid (indicated here as the Maxwell mount of type A – Fig. 11), and
- the case when the normals to the planes containing the contact force vectors bisect the angles of the coupling triangle (indicated here as the Maxwell mount of type B – Fig. 12).

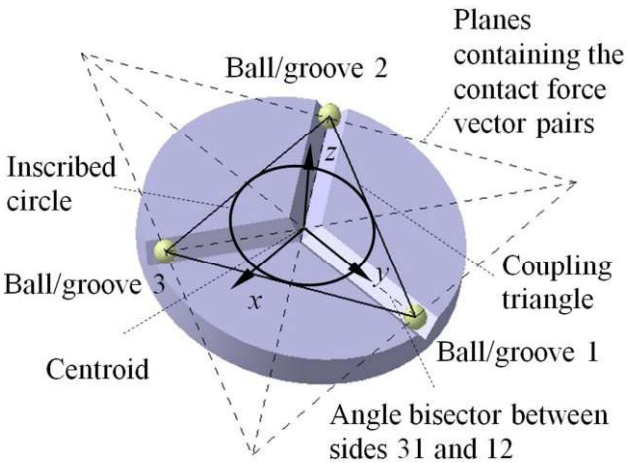

Figure 10. Isometric view of the geometry of the mount.

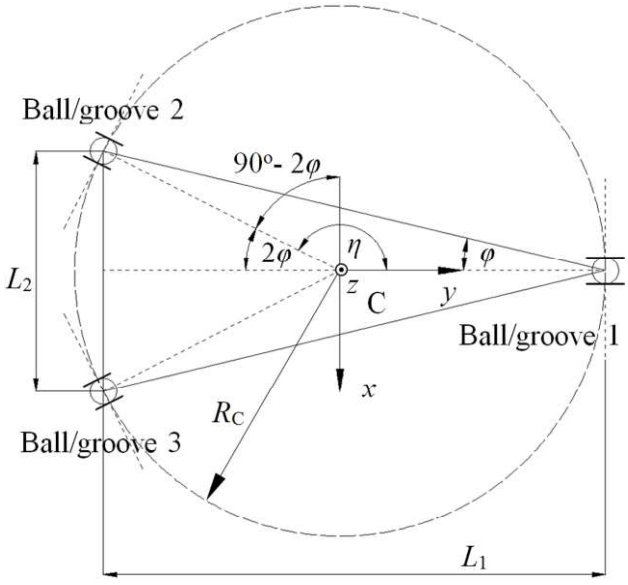

Figure 11. Coupling design configuration type A.

It is to be noted here that the geometry of these two design configurations of the mount are linked to the definition of an auxiliary angle η and the length-to-width ratio of the mount itself. η corresponds to the angle between the segment connecting the centroid of the mount with the centre of ball number 1 and that of ball number 2, respectively.

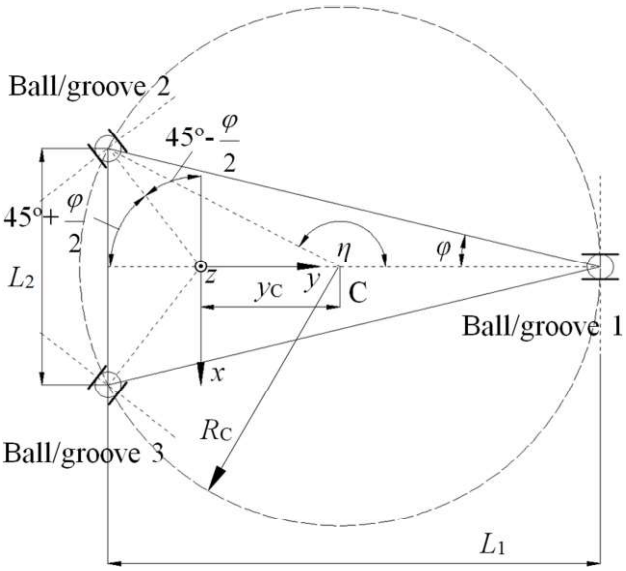

Figure 12. Coupling design configuration type B.

For a known angle η, it stands:

$$\varphi = 90° - \frac{\eta}{2} \tag{12}$$

$$\frac{L_1}{L_2} = \frac{1+\cos 2\varphi}{2\sin 2\varphi} \tag{13}$$

3.1 Coupling design configuration of type A

Based on the design configuration of the Maxwell mount of type A, the coordinates of its contact points and the respective direction cosines of the contact forces are those defined in Table 2.
The resulting force and moment equilibria can be hence defined as:

$$F_{PZ1} + F_{PZ2} + F_{PZ3} - F_{PZ} = 0 \tag{14}$$

$$F_{PZ1}R_C - F_{PZ2}R_C\cos 2\varphi - F_{PZ3}R_C\cos 2\varphi = 0 \tag{15}$$

$$F_{PZ2}R_C\sin 2\varphi - F_{PZ3}R_C\sin 2\varphi = 0 \tag{16}$$

These equilibrium equations define also, as reported in Table 3, the share of the preload (obviously, only in the *z* direction) that each ball will bear.

Table 2. Coordinates of contact points and contact forces' direction cosines – type A Maxwell mount

	Ball 1		Ball 2		Ball 3	
	1	2	3	4	5	6
x_{Ki}	$R_B\cos\alpha$	$-R_B\cos\alpha$	$-R_C\sin2\varphi-$ $-R_B\cos\alpha\cdot\cos2\varphi$	$-R_C\sin2\varphi+$ $+R_B\cos\alpha\cdot\cos2\varphi$	$R_C\sin2\varphi-$ $-R_B\cos\alpha\cdot\cos2\varphi$	$R_C\sin2\varphi+$ $+R_B\cos\alpha\cdot\cos2\varphi$
y_{Ki}	R_C	R_C	$-R_C\cos2\varphi+$ $+R_B\cos\alpha\cdot\sin2\varphi$	$-R_C\cos2\varphi-$ $-R_B\cos\alpha\cdot\sin2\varphi$	$-R_C\cos2\varphi-$ $-R_B\cos\alpha\cdot\sin2\varphi$	$-R_C\cos2\varphi-$ $+R_B\cos\alpha\cdot\sin2\varphi$
z_{Ki}	$-R_B\sin\alpha$	$-R_B\sin\alpha$	$-R_B\sin\alpha$	$-R_B\sin\alpha$	$-R_B\sin\alpha$	$-R_B\sin\alpha$
$\cos\alpha_{Ki}$	$-\cos\alpha$	$\cos\alpha$	$\cos\alpha\cdot\cos2\varphi$	$-\cos\alpha\cdot\cos2\varphi$	$\cos\alpha\cdot\cos2\varphi$	$-\cos\alpha\cdot\cos2\varphi$
$\cos\beta_{Ki}$	0	0	$-\cos\alpha\cdot\sin2\varphi$	$\cos\alpha\cdot\sin2\varphi$	$\cos\alpha\cdot\sin2\varphi$	$-\cos\alpha\cdot\sin2\varphi$
$\cos\gamma_{Ki}$	$\cos\alpha$	$\cos\alpha$	$\cos\alpha$	$\cos\alpha$	$\cos\alpha$	$\cos\alpha$

Table 3. Preload force values on balls – type A Maxwell mount

	Ball 1	Ball 2	Ball 3
F_{Pzi}	$F_{PZ}\dfrac{\cos2\varphi}{1+\cos2\varphi}$	$\dfrac{F_{PZ}}{2(1+\cos2\varphi)}$	$\dfrac{F_{PZ}}{2(1+\cos2\varphi)}$

3.2 Coupling design configuration of type B

In this case it is also necessary to define the coordinates of the coupling centroid C (x_C, y_C, z_C) (cf. Fig. 12) as:

$$C\left(0,\ R_C\left[\cos2\varphi-\sin2\varphi\tan^{-1}\left(45°+\frac{\varphi}{2}\right)\right],\ 0\right) \quad (17)$$

Using again the same approach as in the case of the mount configuration of type A, the coordinates of the contact points and the respective direction cosines of the contact forces can be calculated based on the relations given in Table 4, whereas the shares of the preload that each ball will bear are defined in Table 5.

Table 4. Coordinates of contact points and contact forces' direction cosines – type B Maxwell mount

	Ball 1		Ball 2		Ball 3	
	1	2	3	4	5	6
x_{Ki}	$R_B\cos\alpha$	$-R_B\cos\alpha$	$-R_C\sin2\varphi-$ $-R_B\cos\alpha\sin\xi$	$-R_C\sin2\varphi+$ $+R_B\cos\alpha\sin\xi$	$R_C\sin2\varphi-$ $-R_B\cos\alpha\sin\xi$	$R_C\sin2\varphi+$ $+R_B\cos\alpha\sin\xi$
y_{Ki}	$R_C(1+\cos2\varphi-$ $-\sin2\varphi/\tan\zeta)$	$R_C(1+\cos2\varphi-$ $-\sin2\varphi/\tan\zeta)$	$-R_C\sin2\varphi\cdot\sin^{-1}\zeta\cdot$ $\sin\xi+R_B\cos\alpha\cos\xi$	$-R_C\sin2\varphi\cdot\sin^{-1}\zeta\cdot$ $\cdot\sin\xi+R_B\cos\alpha\cdot\cos\xi$	$-R_C\sin2\varphi\cdot\sin^{-1}\zeta\cdot$ $\sin\xi-R_B\cos\alpha\cdot\cos\xi$	$-R_C\sin2\varphi\cdot\sin^{-1}\zeta\cdot$ $\cdot\sin\xi+R_B\cos\alpha\cdot\cos\xi$
z_{Ki}	$-R_B\sin\alpha$	$-R_B\sin\alpha$	$-R_B\sin\alpha$	$-R_B\sin\alpha$	$-R_B\sin\alpha$	$-R_B\sin\alpha$
$\cos\alpha_{Ki}$	$-\cos\alpha$	$\cos\alpha$	$\cos\alpha\cdot\sin\xi$	$-\cos\alpha\cdot\sin\xi$	$\cos\alpha\cdot\sin\xi$	$-\cos\alpha\cdot\sin\xi$
$\cos\beta_{Ki}$	0	0	$-\cos\alpha\cdot\cos\xi$	$\cos\alpha\cdot\cos\xi$	$\cos\alpha\cdot\cos\xi$	$-\cos\alpha\cdot\cos\xi$
$\cos\gamma_{Ki}$	$\cos\alpha$	$\cos\alpha$	$\cos\alpha$	$\cos\alpha$	$\cos\alpha$	$\cos\alpha$

Table 5. Preload force values on balls – type B Maxwell mount

	Ball 1	Ball 2	Ball 3
F_{Pzi}	$F_{PZ}\frac{\cos 2\varphi}{1+\cos 2\varphi}$	$F_{PZ}\frac{\cos 2\varphi}{1+\cos 2\varphi}$	$F_{PZ}\frac{\cos 2\varphi}{1+\cos 2\varphi}$

Taking into account Equation (14), in this case, the force and moment equilibria will be given accordingly as:

$$F_{PZ1}R_C\left[1+\cos 2\varphi-\frac{\sin 2\varphi}{\tan\varsigma}\right]-F_{PZ2}\frac{R_C\sin 2\varphi}{\tan\varsigma}- \\ -F_{PZ3}\frac{R_C\sin 2\varphi}{\tan\varsigma}-F_{PZ}R_C\left[\cos 2\varphi-\frac{\sin 2\varphi}{\tan\varsigma}\right]=0 \quad (18)$$

$$F_{PZ2}\frac{R_C\cos 2\varphi}{\tan\varsigma}-F_{PZ3}\frac{R_C\cos 2\varphi}{\tan\varsigma}=0 \quad (19)$$

In the above relations, the geometrical parameters ζ and ξ are defined as:

$$\varsigma=45^\circ+\varphi/2 \quad (20)$$

$$\xi=45^\circ-\varphi/2 \quad (21)$$

4 Application of stability analysis and discussion

The outlined Maxwell design configurations of type A and B with their corresponding geometric parameters are used next to assess the stability and behaviour of a factual kinematic mount used to support a large vacuum chamber at a particle accelerator facility. In fact, as extensively elaborated in [12], these types of devices are characterized by extremely stringent design requirements in terms of their positioning and repositioning accuracies and precisions, while being subjected to several sources of external loads such as, for example, those resulting from vacuum loads on the bellows connecting the chamber to the remaining structure of the accelerator.

In the considered case, the input design data are:

- the preload force (mass of the apparatus laying on the mount): F_P = 5 kN,
- externally applied load: F_L = 300 N – acting parallel and vertically shifted by z_L = 1500 mm with respect to the plane of the mount itself, whereas the coordinates x_L and y_L (cf. Fig. 3) can vary depending on the use of the chamber,
- balls' material: silicon nitride (Si_3N_4),
- material of the grooves: tungsten carbide (WC),
- maximum coupling radius: R_{Cmax} = 500 mm.

The unknowns are:

- the radii of the balls R_B, and
- the actual coupling radius R_C.

Considering these unknowns, there are several solutions that comply with the given requirements of system stability and allowable stresses.

In a first instance, the dimensions of the elements of the coupling pair (i.e. the balls and the grooves) are determined on a symmetric configuration of the Maxwell-type kinematic mount. As stated above, this is done based on the polynomial approximation method suggested in [4].

Therefore, Fig. 13 depicts the maximum values of the contact stress q_{max} depending on the radius of the coupling R_C (that is varied in the range from 50 to 450 mm) and the dimension of the balls R_B (varied in the range from 17 to 20 mm). Bearing in mind that the maximal allowable stresses q_{all} should be smaller than 70% of the smallest of the allowable Hertzian contact stresses as defined in the catalogues of the manufactures of the used balls (σ_{Hmax_Si3N4} = 3333 MPa [13]) and grooves (σ_{Hmax_WC} = 4808 MPa [14]), the obtained results imply that the radius of the used balls should be at least R_B = 18 mm. Taking into account Equation (2) and the condition γ = 0,2, the respective V-groove arch radius is hence necessarily R_G = - 21,6 mm. These conditions are thus satisfied for all kinematic mount design configurations for which the overall coupling radius is larger than R_C = 250 mm.

A check is made also to verify whether the position of the external load F_L along the y axis of the mount (i.e. a change of its y_L coordinate) influences the stability of the mount. It could be hence established that this is not the case, i.e., that for all kinematic mount design configurations satisfying the conditions of Fig. 13 the mounts will be stable.

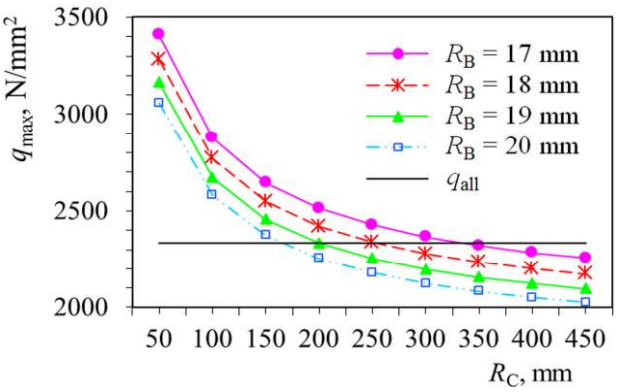

Figure 13. Dimensioning of the elements of the considered kinematic mount.

Ultimately, considering the influence of the kinematic mount design configurations of type A and type B on the stability of the mount, depending on the orientation and the point of application of the external load F_L, typical illustrative results are depicted in Figs. 14-17. The stability regions are here obtained for both considered design configurations in the case when the lateral load passes through the centroid of the kinematic mount but:

- F_L points in the direction of the positive x axis (Fig. 14 – this case is, obviously, mirrored in its effects if F_L points in the direction of the negative x axis),
- F_L points in the direction of the positive y axis (Fig. 15),
- F_L points in the direction of the negative y axis (Fig. 16).

Depending on the aspect ratio of the mount itself, defined by the angle η for a fixed coupling radius R_C = 300 mm, these figures therefore show the critical contact forces which tend to become negative, thus hindering the stability of the mount. Obviously, the contact force(s) significant for the loss of the stability of the mount will, as shown in the figures, be different for the different considered loading cases, whereas the stability region shown in the figures could be increased within the defined allowable range, in the coupling radius R_C. The forces F_{Ki} indicated in the figures are those shown in Fig. 3, i.e., the index "K" indicates contact forces across the ball-to-groove interface, whereas index "i" relates to the contact position. For instance, i = 1 or i = 2 indicate thus the contacts of ball number 1 (cf. Fig. 9) with the respective groove, i = 3 and i = 4 relate to the contact forces of ball no. 2 and so on.

In the case of Fig. 14, it is clear that the mounts in both considered design configurations will be stable in the range of geometries of the mounts for which $95° \leq \eta \leq 145°$, whereas outside of this region the mount will have the tendency to lose contact in either ball 1 or ball 2. On the other hand, when the bounds of the stability region are approached, the forces on ball 3 can approach the values which would result in stresses higher than the determined allowable limit for the used balls q_{all} = 2333 MPa. In these cases, the material of the balls should be changed (the tungsten carbide used for the grooves could already be a satisfactory ball material).

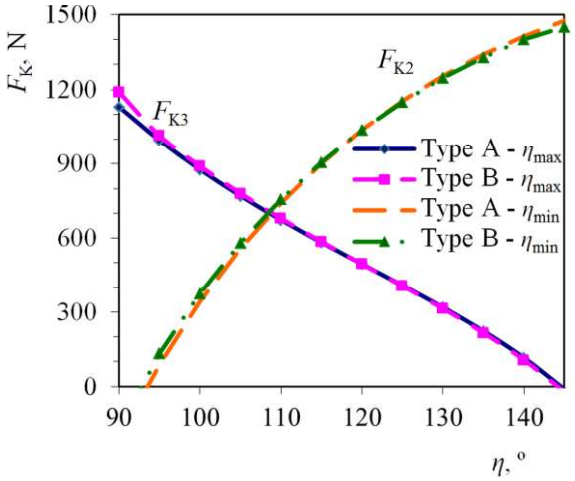

Figure 14. Stability regions when F_L points in the direction of the positive x axis.

When F_L points in the direction of the positive y axis (Fig. 15), the mounts in both considered design configurations will, in turn, be stable in the range of geometries of the mounts for which $73° \leq \eta \leq 171°$, although, obviously, cases with $\eta < 90°$ physically do not make much sense since they would imply that already the weight of the supported apparatus (i.e. the preload F_P) induces a tendency to lift the mount from ball no. 1. Additionally, in this case when $\eta < 135°$, the stresses in ball no. 1 will be higher than allowable, making thus either the modification of the ball material necessary or, as a viable alternative, an increase in the ball radii. In any case, given the resulting rather limited stability range ($90° \leq \eta \leq 135°$), this configuration might therefore, be avoided.

Lastly, when F_L points in the direction of the negative y axis (Fig. 16), the mounts in both considered design configurations will be stable in the range of geometries of the mounts for which

$107° \leq \eta \leq 174°$ (tending, as expected, to loose contact at the balls 2 and 3). In this case the condition of maximal balls' stresses does not impose any bounds on the usable configurations. Most importantly, it is clear here (as visible also in Fig. 15) that in the case of the Maxwell kinematic mount of type B, the stability range tends to increase at its upper bound. This proves, as postulated in [4] that, in the case of couplings with base triangles of larger aspect ratios, the design configuration where the normals to the planes containing the contact force' vectors bisect the angles of the coupling triangle, i.e., indeed, the configuration of type B tends to be a preferable solution.

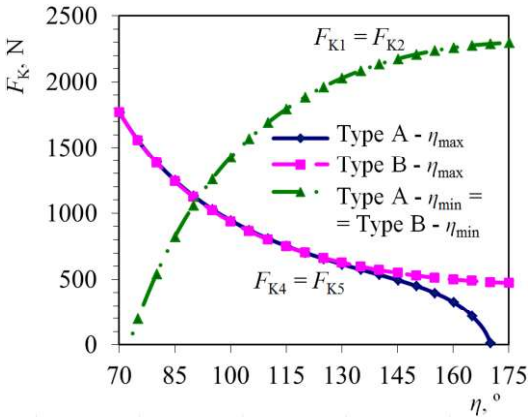

Figure 15. Stability regions when F_L points in the direction of the positive y axis.

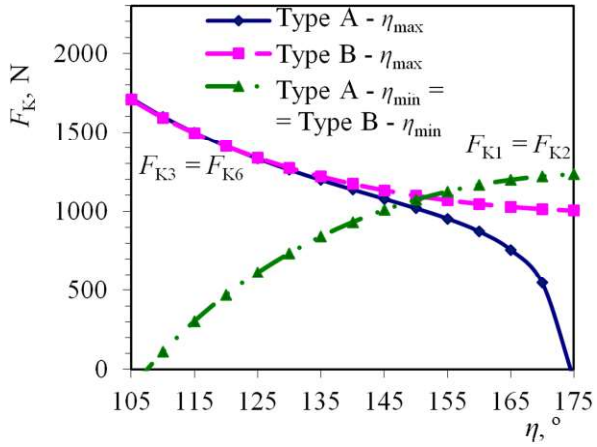

Figure 16. Stability regions when F_L points in the direction of the negative y axis.

As a further interesting variant, Fig. 17 shows how variations of the angle η and of the direction of the lateral load F_L with respect to the y axis of the mount (i.e., of the angle β_L shown in Fig. 3), in the case of the Maxwell kinematic mount of type B affect the value of the contact force F_{K2}, i.e., the respective stability region of the considered design configuration.

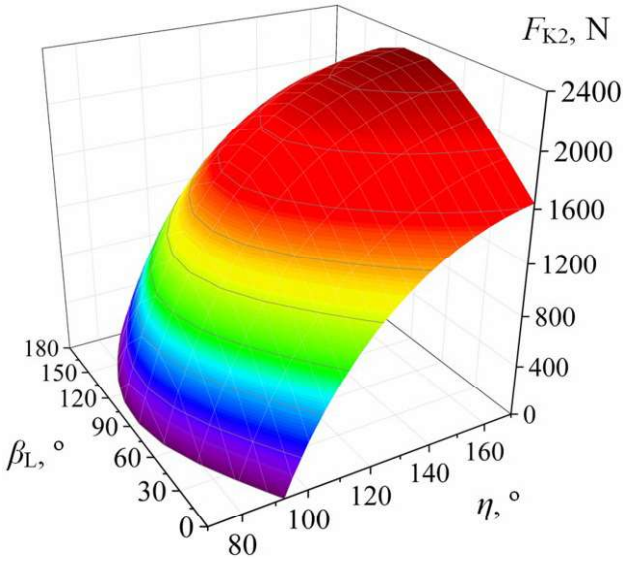

Figure 17. Variation of the contact force F_{K2} for the design configuration of type B depending on the angles η and β_L.

Considering the outcomes of the stability analysis, it was thus possible to substantiate further the hypothesis that when the length of the mount is extended with respect to its width, the Maxwell kinematic mount design configuration of type B is generally better.

5 Conclusions

Thorough analyses of the precision and the stability of Maxwell-type kinematic mounts is performed in this work.

In terms of the stress-strain behaviour in the ball – V-groove contact region, which is closely related to the precision of the considered type of machine elements, it is shown that, except for the gap–bending hypothesis method, the approximated analytical approaches available in literature are giving accurate results in the micrometric and sub-micrometric domain. Experimental measurements of the whole range of elastic deformations allow, in turn, for establishing that the correspondence of theoretical values with the experimental ones is within the intervals of uncertainty of the

measurements, regardless of used materials and lubrication conditions. The repeatability of the kinematic mounts is thus shown to be comparable to the surface finish of the used elements, i.e., in the nanometric domain.

In terms of the stability of the Maxwell-type kinematic mounts, various design configurations and lateral load conditions are considered. Suitable algorithms are implemented and hence applied to a factual design example. It is thus shown that, when the aspect ratio of mount's layout is increased, the Maxwell-type design configuration where the normals to the planes containing the contact forces bisect the angles between the balls is generally better than design configurations where the normals are directed towards the centroid of the coupling.

Acknowledgments

This work is supported by the University of Rijeka scientific grant 13.09.1.2.09 "Characterisation and Modelling of Materials and Devices for Innovative Applications".

References

[1] Marković, K., Franulović, M.: *Contact stresses in gear teeth due to tip relief profile modification*, Eng. Rev., 31 (2011), 1, 19-26.

[2] Lovrin, N., Franulović, M., Vrcan, Ž.: *Some considerations on the load capacity of integral high transverse contact ratio involute gearing*, Eng. Rev., 29 (2009), 2, 53-61.

[3] Hertz, H.: *Gesammelte Werke – Band I.*, J. Ambrosius Barth, Leipzig (D), 1895.

[4] Slocum, A. H.: *Precision machine design*, Prentice Hall, ISBN 0-13-690918-3, New Jersey (NJ, USA), 1992.

[5] Harris, T. A.: *Rolling bearing snalysis – 3rd ed.*, John Wiley & Sons, Inc., ISBN 0-471-51349-0, New York (NY, USA), 1991.

[6] Zelenika, S.: *Analytical and experimental characterization of ball-groove contact problems*, Proc. ATDC'04, Split (HR), 2004, 75-80.

[7] De Bona, F., Zelenika, S.: *A generalized elastica-type approach to the analysis of large displacements of spring-strips*, J. Mech. Eng. Sci. – Proc. Ins. Mech. Eng. C, 211 (1997), 509-517.

[8] Timoshenko, S. P., Goodier, J. N.: *Theory of elasticity*, 3rd edition, McGrawHill, ISBN 0-07-07-2541-1, New York (NY, USA), 1970.

[9] Young, W. C.: *Roark's formulas for stress and strain*, McGrawHill, ISBN 0-07-100373-8, New York (NY, USA), 1989.

[10] Jacazio, G., Piombo, B.: *Meccanica applicata alle macchine*, Levrotto & Bella, Torino (I), 1992.

[11] Jacazio, G.: *Progettazione delle strutture meccaniche*, Eda, Torino (I), 1985.

[12] Zelenika, S.: *Mechanical aspects of the design of 3rd generation synchrotron light sources,* CAS – CERN Accelerator School: Synchrotron Radiation and Free-Electron Lasers, Brandt, D. (Ed.), CERN, Geneva (CH), 2005, 337-362.

[13] *www.esk.com/en/downloads/technical-data-sheets.html*

[14] *www.gimex.nl/english/index.html*